17 Feb 2022

Effect of Processing Parameters and Build Orientation on Microstructure and Performance of AISI Stainless Steel 304L Made with Selective Laser Melting under Different Strain Rates

Tan Pan

Xinchang Zhang

Aaron Flood

Sreekar Karnati

et. al. For a complete list of authors, see https://scholarsmine.mst.edu/matsci_eng_facwork/2895

Recommended Citation

T. Pan et al., "Effect of Processing Parameters and Build Orientation on Microstructure and Performance of AISI Stainless Steel 304L Made with Selective Laser Melting under Different Strain Rates," *Materials Science and Engineering A*, vol. 835, article no. 142686, Elsevier, Feb 2022.
The definitive version is available at https://doi.org/10.1016/j.msea.2022.142686

Materials Science & Engineering A 835 (2022) 142686

Contents lists available at ScienceDirect

Materials Science & Engineering A

journal homepage: www.elsevier.com/locate/msea

Effect of processing parameters and build orientation on microstructure and performance of AISI stainless steel 304L made with selective laser melting under different strain rates

Tan Pan [a,*], Xinchang Zhang [a], Aaron Flood [a], Sreekar Karnati [a], Wei Li [b], Joseph Newkirk [c], Frank Liou [a]

[a] Department of Mechanical & Aerospace Engineering, Missouri University of Science and Technology, Rolla, MO, 65409, USA
[b] Department of Mechanical Engineering, University of Texas at Dallas, Richardson, TX, 75080, USA
[c] Department of Materials Science & Engineering, Missouri University of Science and Technology, Rolla, MO, 65409, USA

ARTICLE INFO

Keywords:
Selective laser melting
Stainless steel 304L
Strain rate sensitivity
Material characterization
Mechanical anisotropy

ABSTRACT

Selective laser melting (SLM) process allows greater geometry flexibility; therefore, it has become more widespread in its deployment in the industry for fabricating metal alloys. However, a material characterization study is needed in order to understand better the correlation between the process, microstructure, and performance. In the current study, the raw SLM fabricated AISI stainless steel 304 L was fabricated with different processing parameters and build orientations (horizontal, inclined, and vertical). The tensile behavior was evaluated under different strain rates (0.0001/s, 0.001/s, 0.01/s, and 0.1/s) and then compared to commercial cold-rolled and annealed counterparts. Grain structures, tensile strength, elongation-to-failure, strain rate sensitivity, work hardening, and fractographic analysis were evaluated in terms of the effect of energy density, build orientation, and strain rate. The results indicate that the tensile strength increases with increasing strain rates. On the contrary, the elongation-to-failure shows a decreasing trend with strain rates. Tensile properties of specimens built in the horizontal and inclined orientations are more sensitive to strain rates due to the smaller dimension of grain structures. Tensile anisotropy depends on the energy input, where a high energy density could yield a strong build orientation-dependent anisotropy. The Hall-Petch relationship is validated to explain the mechanical anisotropy in different build orientations for SLM samples. The strain hardening exponent and work hardening rate are revealed to be positively correlated, and both of them increase with smaller grain sizes. The fine dimple features indicate the ductile fracture mode regardless of strain rates. The size of the ductile dimples seems to depend on the strain rates and build orientations.

1. Introduction

Additive manufacturing (AM), as an emerging metal manufacturing method, is unique. Unlike conventional manufacturing (i.e., casting) where an intensive and costly post-machining is required to subtract materials, AM enables the additive fabrication of metal alloys with a layer-by-layer nature. The design freedom resulting from AM offers an opportunity to generate complex geometries and reductions in weight with less post-machining and assembling process. However, the current cost of feedstock for AM is expensive, especially for powder bed fusion (PBF), where the size and morphology of the feedstock material are highly specific. Studies on the reduction of the feedstock cost are advancing to help facilitate the broader adoption of AM [1]. For metal AM fabrications, two strategies are commonly applied: directed energy deposition (DED) and PBF system. DED employs a heat source to melt the metallic feedstock (i.e., powder or wire) feed into the molten pool. The flexible feeding system of DED allows the application for remanufacturing defective but costly components (i.e., dies, molds) [2,3] and depositing functionally gradient materials [4,5]. For the PBF system with selective laser melting (SLM) process, the powder particles are placed on the substrate with thin layer thickness and melted by the energy source (i.e., laser or electron beam) based on the sliced geometry of each layer. PBF systems have an extraordinary potential to create complex geometries due to their accuracy. However, the densification,

* Corresponding author.
E-mail address: tpb44@mst.edu (T. Pan).

https://doi.org/10.1016/j.msea.2022.142686
Received 11 November 2020; Received in revised form 21 December 2021; Accepted 16 January 2022
Available online 19 January 2022

microstructure, and mechanical performance of the AM metal alloys are profoundly affected by the parameters of the AM process. Inappropriate processing parameters introduce defects like porosity, delamination, deflection, and microcracks, which could vastly deteriorate tensile properties, hardness, toughness, and fatigue performance.

Austenitic stainless steel is one of the most popular classes of metallic materials, which has been broadly applied in various industries. Among those, austenite stainless steel AISI 304 L (SS 304 L) is featured with a high corrosion resistance by the addition of chromium. Besides, SS 304 L has comparable tensile strength when compared to SS 316 L [6,7], which makes it a desirable candidate for implementation in the nuclear and automobile industries [8]. AM, as a new solution to fabricate this type of stainless steel and its close relatives, has been developed to demonstrate the feasibility and establish the relationships among process, microstructure, and performance by many researchers. Guan et al. [9] showed the tensile properties of SLM SS 304 slowly increased with an interval number of the deposited layer. The impact of hatch angle and anisotropy of build orientations on tensile performances was demonstrated. They also exhibited a higher tensile performance for SLM material when compared to its wrought counterpart. Nguyen et al. [10] explained the strengthening mechanisms behind the SLM material, which is attributed to the formation of nano-cellular structures, grain refinement due to the fast cooling rate and the solidification process (Hall-Petch effect), the formation of martensite phase, and the negative residual stress induced by the micro-shrinkage in every single layer during solidification. Wang et al. [11] elucidated the effect of process parameters on the anisotropic and heterogeneous microstructure and tensile mechanical properties. They pointed out the tensile properties were higher in the lower linear heat input, which had a finer microstructure, in comparison to the higher linear heat input.

Strain rate sensitivity studies were carried on for conventional wrought austenitic stainless steel, where the deformation-induced α'-martensite formation (DIMF) occurs during plastic deformation within certain temperature ranges, denoted as M_s (lower limit) and M_d (upper limit). The low stacking fault energy (SFE) of austenitic stainless steel promoted the formation of shear bands consisting of stacking fault bundles and deformation twins at the early stage of deformation. The α'-martensite is a body-centered cubic (BCC) as opposed to austenite, which is a face-centered cubic (FCC). The BCC structure can nucleate at the intersections of shear bands at a temperature range between M_s and M_d [12–15]. Angle [16] proposed an empirical equation in terms of chemical composition to determine M_{d30} as the temperature where 50% in volume of the austenite transforms to martensite with an applied true strain of 30% as following Eq. (1).

$$M_{d30}(^{\circ}C) = 413 - 462(C+N) - 9.2Si - 8.1Mn - 13.7Cr - 9.5Ni - 18.5Mo \quad (1)$$

where the elements are in weight percentage. The formed deformation-induced α'-martensite enhances the work hardening, leading to higher tensile strength and postpone plastic instability [17]. When the α'-martensite forms at high strains, it improves the ductility by preventing the onset of necking, which is referred to as transformation induced plasticity effect (TRIP) [18,19]. Strain rate positively affects the amount of α'-martensite formation during deformation [14,20]. However, the increasing strain rate, along with the adiabatic heating stabilizes the austenite and suppresses the DIMF [15].

The processing parameters significantly influence the microstructure and performance of the final specimens due to the complicated melting and solidification mechanisms of the SLM process. For safety concerns, it is imperative to characterize the SLM products comprehensively before industry adoption. Although the impact of process parameters on the tensile properties for SLM SS 304 L has been established for static loading applications, the performance of SLM metals with varying processing parameters is still insufficient for different loading applications over a wide range of strain rates. In the current study, SS 304 L, typical austenitic steel with considerable industrial applications, was selected to be fabricated with the SLM process with different process parameters. The cold-rolled and annealed counterparts were tested as a baseline for the AM results. Characterizations of tensile performance were conducted over a wide range of strain rates (0.0001/s, 0.001/s, 0.01/s, and 0.1/s). The main focus of the testing was on the establishment of the relationship between processing parameters, microstructure, and performance under different test rate conditions. The output from the current study quantitatively highlights the connection between microstructure, tensile properties, strain rate sensitivity, work hardening, and fracture mechanism with building conditions and discusses the anisotropic properties of SLM fabricated alloy in terms of input energy/process parameter, and build orientations (horizontal, inclined, and vertical).

2. Experimental procedure

2.1. Material

The target material investigated in this study is the SS 304 L. Argon gas-atomized SS 304 L powder was procured from LPW technology Ltd with the chemical composition listed in Table 1, quantified by Inductively coupled plasma - optical emission spectrometry technique by the powder supplier. The commercially purchased wrought SS 304 L in cold-rolled and annealed state was studied as the baseline fabricated with conventional manufacturing method with the elemental composition tabulated in Table 1.

2.2. Selective laser melting process

The Renishaw AM 250, which is a laser-based powder bed fusion system, was used to produce in the current study to print the samples. A schematic of the building process is shown in Fig. 1a. The AM 250 adopts a spot-by-spot melting method. Hence, the densification largely depends on the overlap between successive laser scans and consecutive layers. The Renishaw AM 250 is equipped with a 200 W Nd-YAG pulsed laser with a Gaussian beam profile. A plain carbon steel plate was used as the substrate material. During the printing process, the substrate plate and the powder were kept to 80 °C to reduce the moisture inside the chamber. The oxygen level was maintained below 1000 ppm inside the building chamber to mitigate the material oxidation during the laser melting process. A constant volumetric argon gas flow was sustained to remove the ejecta or condensate generated during the building process.

Due to differing definitions of energy density, it is necessary to define which method was used. The most common definitions found in the literature are linear energy density [11], which only depends on laser power and scan speed, volumetric energy density [22], and normalized energy density, which includes the thermophysical properties of as-built materials [23]. In this study, the volumetric energy density is applied and is defined as Eq. (2).

$$ED = \frac{P}{v^* h^* t} \quad (2)$$

where P is the laser power in W, v is the scan speed in m/s, h is hatch spacing in mm, and t is layer thickness in mm. This definition was chosen because it includes hatch spacing, which is the main focus of this study. The pair of energy densities used in this study are listed in Table 2, and a diagram is plotted to illustrate the corresponding processing parameters in Fig. 1b. The difference between low energy density (LED) and high energy density (HED) is the varying hatch spacing, which is defined as the distance between two successive laser scans. Hatch spacing describes the extent of overlap between two scan tracks. The insufficient overlap could give rise to the lack of fusion porosity. In contrast, excessive overlap can cause over-melting, which can increase keyholing or gas porosity. Hence a precise control of hatch spacing is essential for

Table 1
The chemical composition of stainless steel 304 L in cold-rolled and annealed state and stainless steel 304 L powder particle in weight percentage.

Element	C	Cr	Cu	Fe	Mn	N	Ni	O	P	S	Si
Wrought	0.030	18–20	–	Bal.	2	0.01	8–12	–	0.045	0.03	1
Powder	0.018	18.4	<0.1	Bal.	1.4	0.06	9.8	0.02	0.012	0.005	0.6

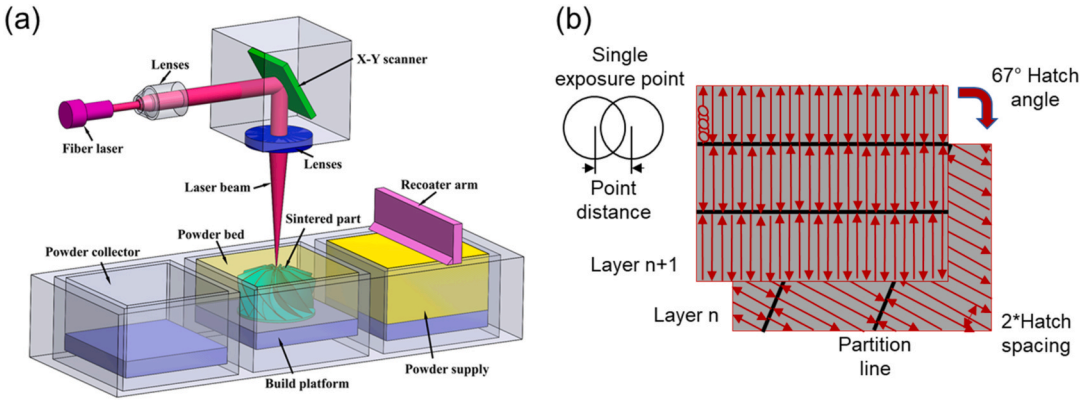

Fig. 1. (a) The schematics of the SLM process; (b) Stripe scan strategy with corresponding build process parameters.

Table 2
The process parameters in terms of LED and HED used for the fabrication.

Parameter	LED	HED
Laser power (W)	200	200
Layer thickness (μm)	50	50
Point distance (μm)	70	70
Hatch spacing (μm)	85	65
Scan speed (m/s)	0.8	0.8
Spot diameter (μm)	70	70
Exposure time (μs)	88	88
Energy density (J/mm^3)	58.8	76.9

building high-quality components. The rest of the applied processing parameters were studied in the preliminary study and experimentally validated that good densification and mechanical performance were achieved by these parameters [7,21]. A stripe scan strategy was adopted in this study with a 67° hatch angle between consecutive layers to avoid the inherent residual stress built up in one direction.

2.3. Material characterization

Samples were printed in horizontal (0°), inclined (45°), and vertical (90°) orientations, as depicted in Fig. 2a. The dimension of the block specimen was designed to be 12 mm (in the x-direction) * 12 mm (in the y-direction) * 57 mm (in the z-direction). The sample surfaces of as-built samples were ground with SiC sandpaper (400, 600, 800 and 1200 grit). Density testing was further performed to confirm the high densification of the printed materials. Density was evaluated using the Archimedes principle with deionized water as the liquid medium. Longitudinal and transverse cross-sections were revealed by using the Sodick VZ300L Wire Electric discharge machine (EDM) to section the pieces of the specimens. The cross-sections in different build orientations were then mounted in conductive Bakelite, ground, and polished following the standard procedure. Electron backscatter diffraction (EBSD) was performed to reveal the growth orientations of the grain structures and determine the average grain sizes with different building conditions with a dual-beam scanning electron microscope (SEM, FEI Helios Nano 600). The scan was acquired with an Oxford HKL system with a step size of 1.25 μm. The visualization of EBSD data was performed by HKL Channel 5 software. The line intercept method was applied to quantify the average grain size.

The miniature tensile specimen [24] was used in this study under uniaxial tensile testing. The dimensions of the miniature specimens are shown in Fig. 2b, with a gauge length of 3.00 mm. The tensile specimens were sectioned from the built block and machined to size with EDM, with the loading direction perpendicular (horizontal), 45° inclined (inclined), and parallel (vertical) to the build orientation (z-direction in Fig. 2a) as depicted in Fig. 2a. Before testing, the specimens were ground with 800-grit SiC sandpaper. An Instron 5969 machine (Instron, Norwood, MA, USA) was employed to conduct the uniaxial tensile testing at room temperature. The tensile testing was operated by the constant test speed of 0.0003, 0.003, 0.03, and 0.3 mm/s to impose four orders of

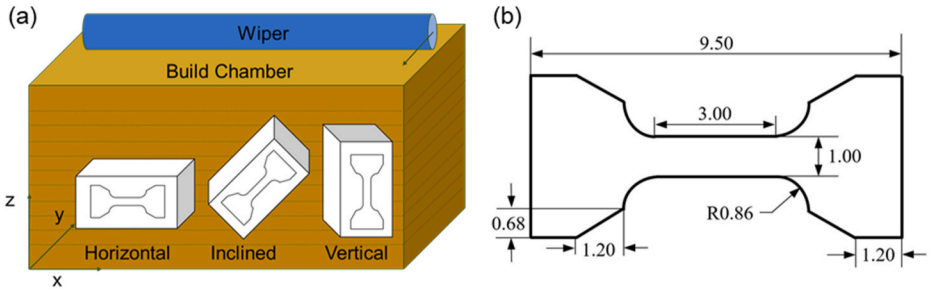

Fig. 2. (a) The build of fabricated specimens in horizontal, inclined, and vertical orientations where z-direction represents the build direction, and (b) the dimension of the miniature tensile specimens in mm [24].

strain rates of 0.0001, 0.001, 0.01, and 0.1/s. Extensometer feedback was applied until a strain value of 30%. At least five specimens in different manufacturing states were tested per each test speed. The fracture surfaces of the broken miniature tensile specimens were examined under SEM (FEI Helios Nanolab 600 and Aspex 1020).

3. Results

3.1. Density and microstructure

The density of the SLM SS 304 L printed with the LED and HED parameters was determined in different orientations with the result tabulated in Table 3 where LED and HED are defined above as the processing parameters energy levels. The appended "H", "I", and "V" stand for the horizontal, inclined, and vertical build orientation, respectively. The powder has a true density of ~7.93 g/cm^3 according to the supplier. Hence, the block specimens in different building conditions exhibit densifications of ~99%.

The examination of the microstructures of SS 304 L is shown in Fig. 3 and Fig. 4, for specimens built using the LED and HED processing parameters, respectively. To determine the average grain size, the high angle grain boundary (highlighted in Figs. 3 and 4) with a misorientation of 15° was used. The determined average grain size is listed in Table 3 for different manufacturing states. For both process parameters, the as-printed SS 304 L mainly consists of γ-austenite matrix with FCC structure, with the little amount of δ-ferrite with a BCC structure (with a volume fraction <1%). A fine equiaxed grain structure with an average size of 5.5 ± 0.4 μm is observed for wrought SS 304 L with the EBSD map shown in Figs. 3d and 4d. The coarse grain structures of additive samples can be perceived when compared to the wrought SS 304 L. The measured average grain sizes are 19.2 ± 17.9 μm in horizontal (H) direction, 19.7 ± 8.2 μm in inclined (I) direction, and 27.4 ± 12.9 μm in vertical (V) direction for the LED process parameter, while 21.1 ± 7.1 μm (H), 20.4 ± 6.7 μm (I), and 29.2 ± 22.6 μm (V), for the HED process parameter. Figs. 3e and 4e show the pole figure of SS 304 L fabricated with SLM, where a predominant crystallographic orientation is along the {100} orientation, which is coincident with the build direction (z-axis in Fig. 2a) with a ~ ±5° deviation. The maximum intensity is ~5.01 and ~5.73 multiples of the uniform density for the LED and HED, respectively.

3.2. Tensile behavior

Fig. 5 illustrates the engineering stress-strain curve for wrought and SLM SS 304 L built with LED and HED processing parameters in different build orientations and tested at different strain rates. Compared with the SS 304 L fabricated in different methods (i.e., wrought and SLM fabricated), wrought materials possess lower YS while higher UTS than those of SLM SS 304 L due to higher working hardening during plastic deformation. In addition, lower elongation-to-failures were obtained with SLM SS 304 L, especially in inclined and horizontal orientations. In terms of different build orientations, as depicted in Fig. 2a, the specimens built in horizontal and inclined orientations have higher tensile stress than those in the vertical orientation. YS and UTS slightly increase with strain rates from 0.0001/s to 0.1/s. No noticeable correlation between the tensile strain and strain rates can be detected except for the lower elongation-to-failure of wrought specimen tested at 0.1/s.

Table 3
Determined density and average grain size of specimens in different manufacturing state.

SLM fabrication state	Density (g/cm^3)	Average grain size (μm)
LEDH	7.89 ± 0.02	16.5 ± 3.6
LEDI	7.90 ± 0.02	19.7 ± 8.2
LEDV	7.89 ± 0.03	27.4 ± 12.9
HEDH	7.87 ± 0.07	21.1 ± 7.1
HEDI	7.84 ± 0.07	14.7 ± 7.0
HEDV	7.87 ± 0.06	29.2 ± 22.6
Wrought		5.5 ± 0.4

Fig. 6 and Table 4 show the variations of YS and UTS with different strain rates of the wrought specimens and SLM specimens built with LED and HED at different orientations. The general trends of yield strength for both wrought and AM fabricated stainless steel moderately increase with strain rates ranging over four orders of magnitude. For wrought SS 304 L, yield strength rises from 345 ± 12 MPa at 0.0001/s to 413 ± 8 MPa at 0.1/s. A similar phenomenon for the increasing yield strength (Fig. 6a) with strain rates can be summarized for the SLM materials printed with different parameters and orientations. In FCC alloys, an increase in the strain rate could extensively affect the deformation mechanism like the change of dislocation arrangement and dislocation motion [26] and mechanical twinning [27]. For the UTS value, the increasing trend can be observed with strain rates from 0.0001/s to 0.01/s, which is confirmed with both Fig. 6b and the value listed in Table 4. However, the UTS values at the highest strain rate (0.1/s) keep consistent or even lower than those tested at 0.01/s (i.e., wrought, LEDI, and HEDI). Lichtenfeld et al. [15] explained the increase in tensile strength as the deformation-induced martensite transformation was uninhibited at a lower test rate, which increased UTS. However, the self-heating of the test specimens prohibited the martensite transformation and stabilized the austenite phase. Also, the SFE increased with temperature, which diminished the density of planar slip features associated with the nucleation of the martensite. Zhuo et al. [26] demonstrated the comparable results of UTS for SS 316 L. They mentioned the occurrence of inhomogeneous plastic deformation gave rise to the insensitivity of UTS on strain rate at higher test speeds.

It is also interesting to note that SLM-fabricated SS304L built with both parameters possess higher yield strengths than those of the wrought counterparts in an amount of more than 100 MPa for horizontal and inclined orientations. The stronger dislocation barrier of grain boundaries was emphasized compared to cell boundaries [38]. SLM stainless steel could be subject to a strengthening effect due to the unique manufacturing fashion with a rapid solidification rate, which could induce the refinement of grain size, post-deformation annealing, higher dislocation density, dispersion strengthening from nanoscale oxides [28]. However, the wrought SS304L exhibits the highest UTS instead. The intrinsic fabrication fashion of AM methods generates defects (i.e., porosity, inclusion, and micro-void) during the building process due to the intensive interactions among the laser source, powder, wiper, and flow gas inside the build chamber [39]. The resultant defects could initiate an earlier stage of localized and inhomogeneous deformation (necking effect). Hence the UTS would be lower than that of the wrought counterpart (Fig. 5).

Fig. 7 and Table 5 show the variations of uniform elongation ε_u, where UTS is achieved and elongation-to-failure ε_f, where ultimate fracture occurs, with different strain rates of the wrought specimens and specimens built with LED and HED at different orientations. Neither ε_u nor ε_f show a significant difference with strain rate at lower strain rates (i.e., 0.0001/s to 0.01/s). At the highest strain rate (0.1/s), the ε_u and ε_f suddenly decline. Zhuo et al. [26] explained it as the delayed necking occurred at the lower strain rates. Khodabakhshi [29] pointed out the reduced elongation-to-failure at higher strain rates could be attributed to the dislocation theory. The high dislocation density inside the material becomes brittle after the occurrence of necking instability and, therefore, fractures with lower strain values.

3.3. Fractographic analysis

According to Refs. [36,37], a close correlation between the dimple size on the fracture surface and the intrinsic grain structure is proposed. Fig. 8 shows the overview of the fracture surface and the corresponding

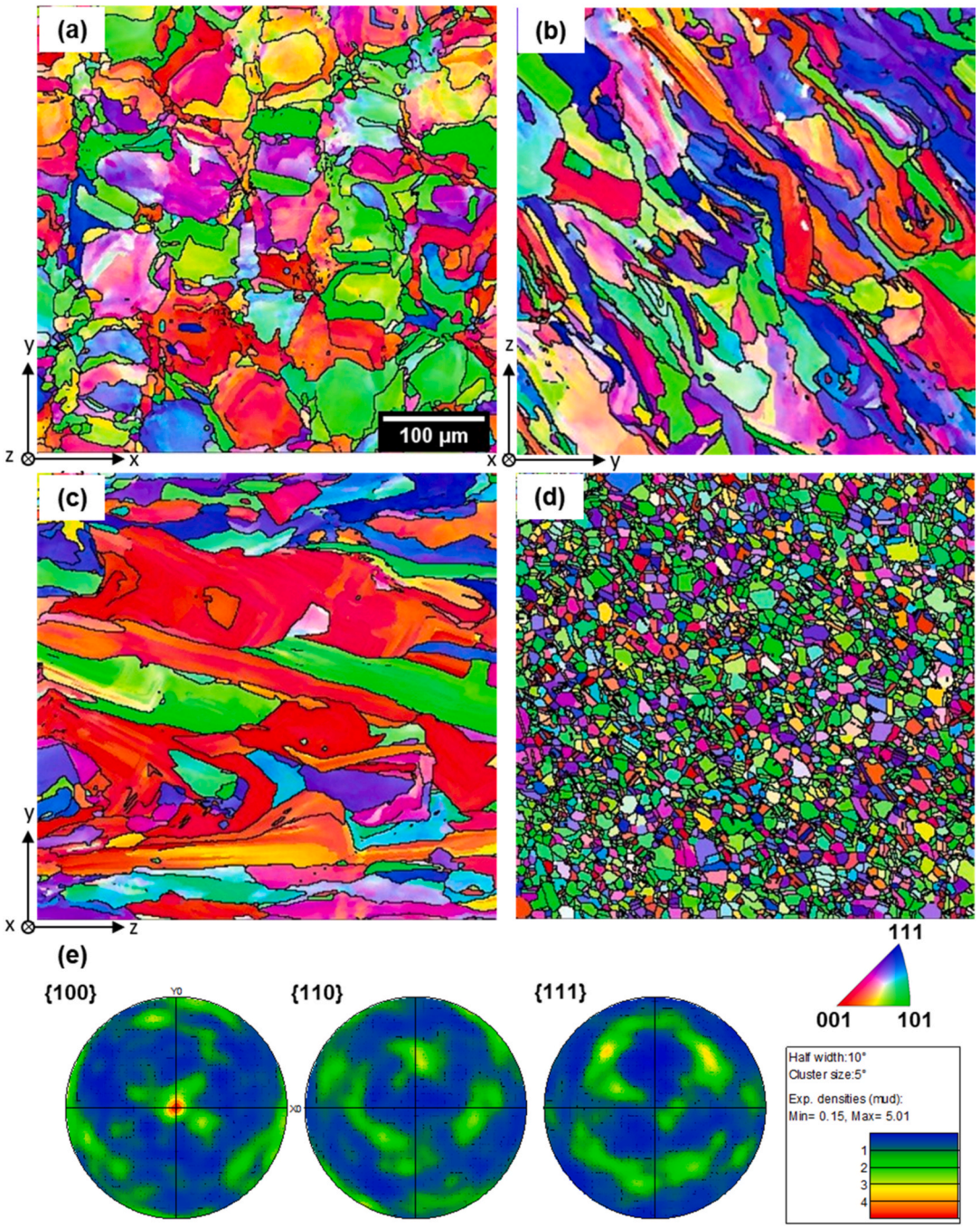

Fig. 3. Inverse pole figure in (a) 0°, (b) 45°, and (c) 90° plane (with arrow indicating the direction) for SS 304 L built in LED and (d) for wrought SS 304 L as a comparison; (e) pole figure of SLM specimen built in LED.

high magnification images of the wrought specimen under tensile testing at different strain rates. The overview images expose the void sheet (in the middle area) and a shear lip zone on the fracture surface. Some void features in the nanoscale are occasionally visible in the matrix on the fracture surface (highlighted in yellow arrows) with an average size of 0.72 µm.

Fig. 9 shows the overview of the fracture surface and the corresponding high magnification images of SLM fabricated specimens built with LED in the different build orientations. The tensile specimens were tested at 0.001/s. The overview images also expose the void sheet (in the middle area) and the shear lip zone on the fracture surface. The coarsening voids can be seen on the fracture surface highlighted with yellow arrows. Relatively large pores and voids with the existence of unmelted powder particles (highlighted with the orange arrow) can be observed for specimens in the horizontal and vertical orientations, which also coarsens during the plastic deformation. The images in high magnification reveal the ductile dimple features in all the orientations, which identifies the ductile fracture mode of the SLM specimen. The size of the dimple is quite similar in horizontal and inclined orientations while a relatively larger size is noticed in the vertical orientation. Table 3 shows a larger grain size in the vertical orientation; hence, a relatively larger size of the dimple is detected than the other orientations. A coarsening micro-void (highlighted with a red arrow) in the matrix is identified on the fracture surface from horizontal orientation, with a size of ~7 µm, where un-melted fine powder particles or nucleated inclusions/condensate could previously locate.

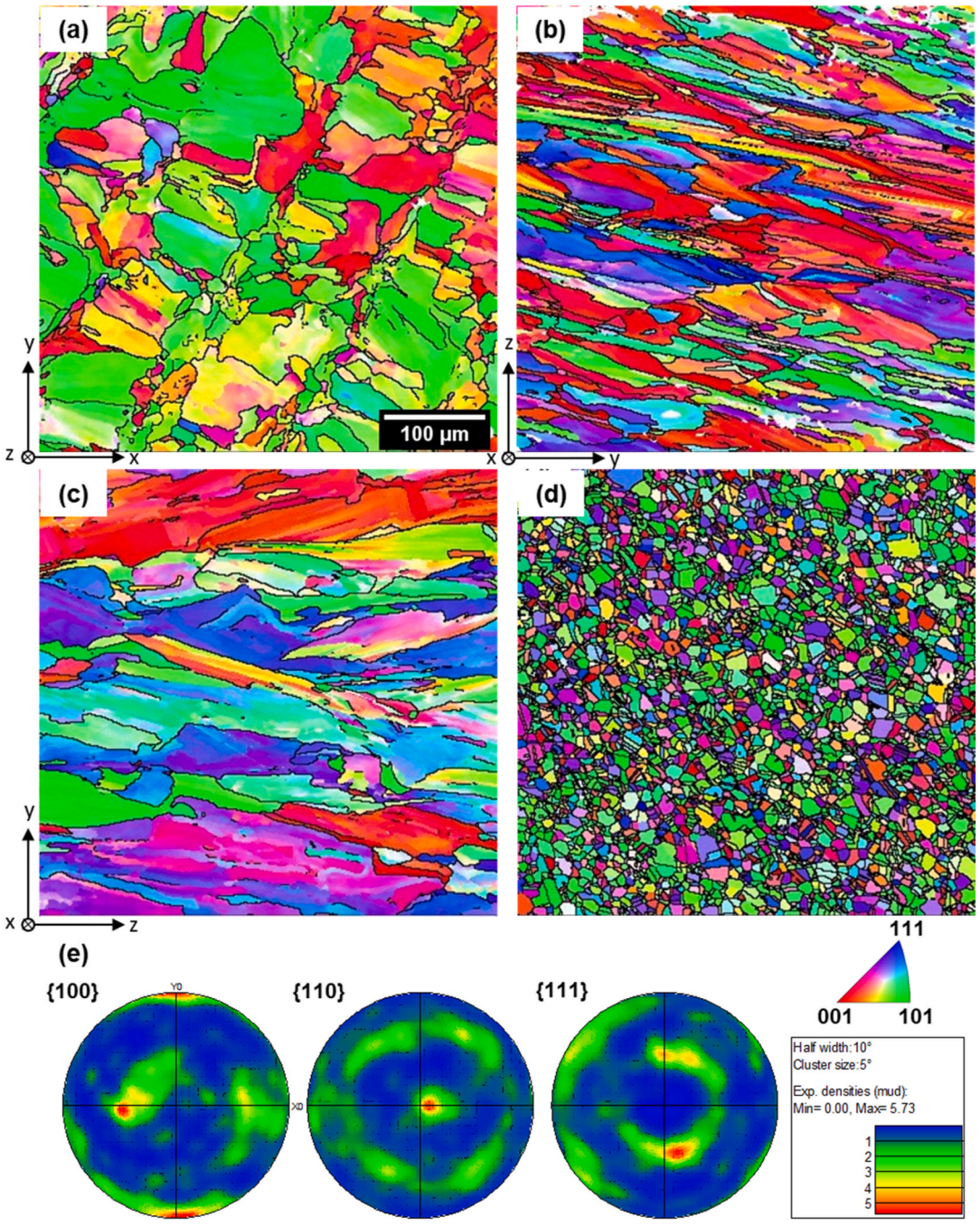

Fig. 4. Inverse pole figure in (a) 0°, (b) 45°, and (c) 90° plane (with arrow indicating the direction) for SS 304 L built in HED and (d) for wrought SS 304 L as a comparison; (e) pole figure of SLM specimen built in HED.

4. Discussion

4.1. Microstructure

The grain structures in the horizontal and inclined orientations are visibly finer than those in the vertical orientation. And, an equiaxed cellular grain morphology is mainly observed in the horizontal orientation. On the contrary, an elongated columnar grain structure is chiefly exhibited in the inclined and vertical orientations due to the direction of grain growth. The relatively weak texture from a low energy input could be attributed to the fact that the reduction of the extent of remelting for the previously printed layer inhibits the epitaxial growth of grains, which permits a relatively uniform distribution [25].

4.2. Strain rate sensitivity

The strain rate sensitivity factor (m) can be defined as Eq. (3) at a constant strain,

$$m = \left(\frac{\partial\, ln\sigma}{\partial\, ln\dot{\varepsilon}}\right) \tag{3}$$

where the σ is the tensile strength and $\dot{\varepsilon}$ is the strain rate. Strain rate sensitivity m determined for different manufacturing states is plotted in Fig. 10. The determined m values are also reported with standard deviation in Table 6 for better interpretation. Wrought SS 304 L performs the highest m (~0.0261), indicating it is most susceptible to strain rates. YS and UTS for wrought material gradually increase with strain rate,

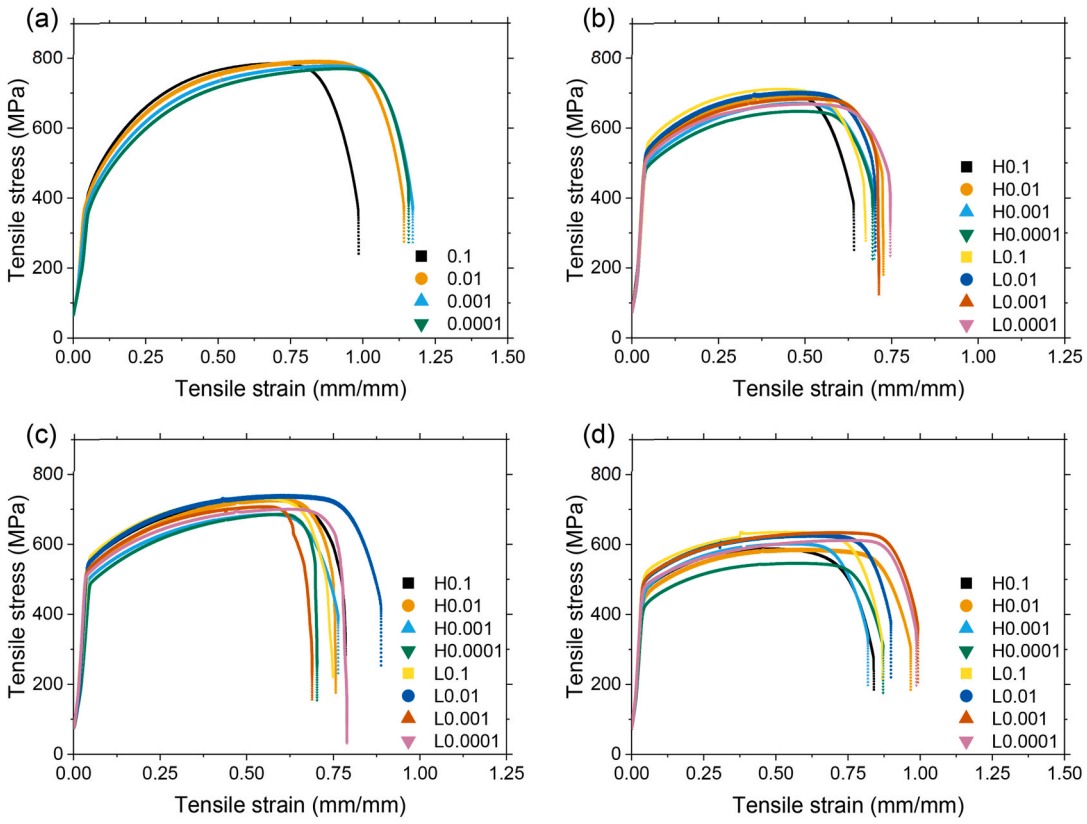

Fig. 5. Engineering stress-strain curve of (a) wrought, and SLM material built with LED (represented by 'L') and HED (represented by 'H') in (b) horizontal, (c) Inclined, and (d) vertical orientations tested at 0.0001 to 0.1/s.

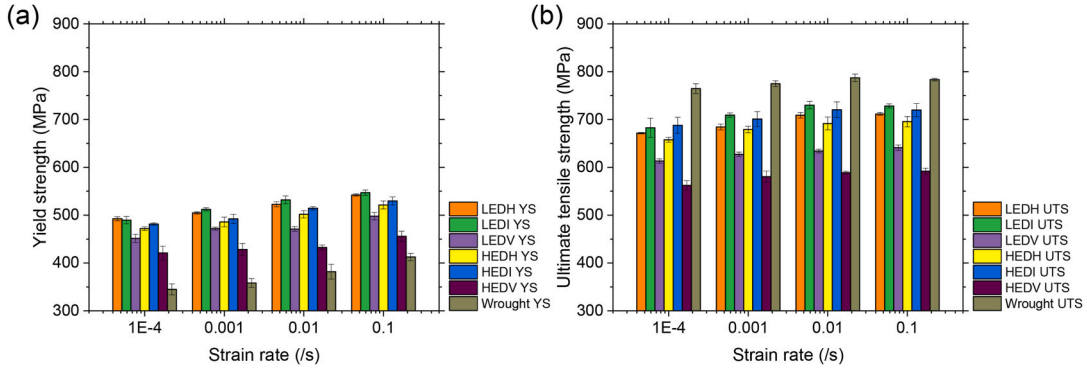

Fig. 6. (a) YS and (b) UTS comparison varied at different strain rates for wrought and SLM materials built with LED and HED in three orientations.

Table 4
Yield strength (YS) and ultimate tensile strength (UTS) value in MPa at different strain rates for wrought and SLM materials built with LED and HED in three orientations.

Manufacturing state	Strain rate (/s)							
	0.0001		0.001		0.01		0.1	
	YS	UTS	YS	UTS	YS	UTS	YS	UTS
Wrought	345 ± 12	765 ± 10	358 ± 9	775 ± 6	382 ± 16	787 ± 8	413 ± 8	784 ± 3
LEDH	492 ± 4	671 ± 2	505 ± 2	684 ± 6	523 ± 5	709 ± 6	542 ± 2	712 ± 3
LEDI	490 ± 8	683 ± 20	512 ± 3	709 ± 5	532 ± 8	730 ± 8	547 ± 6	728 ± 5
LEDV	451 ± 8	613 ± 4	472 ± 3	627 ± 5	481 ± 5	634 ± 4	498 ± 8	641 ± 5
HEDH	472 ± 4	658 ± 5	486 ± 10	679 ± 7	502 ± 8	692 ± 13	521 ± 8	695 ± 11
HEDI	481 ± 2	688 ± 17	492 ± 9	701 ± 16	514 ± 4	721 ± 16	530 ± 8	720 ± 14
HEDV	421 ± 14	562 ± 10	428 ± 12	580 ± 12	443 ± 5	589 ± 3	456 ± 11	592 ± 6

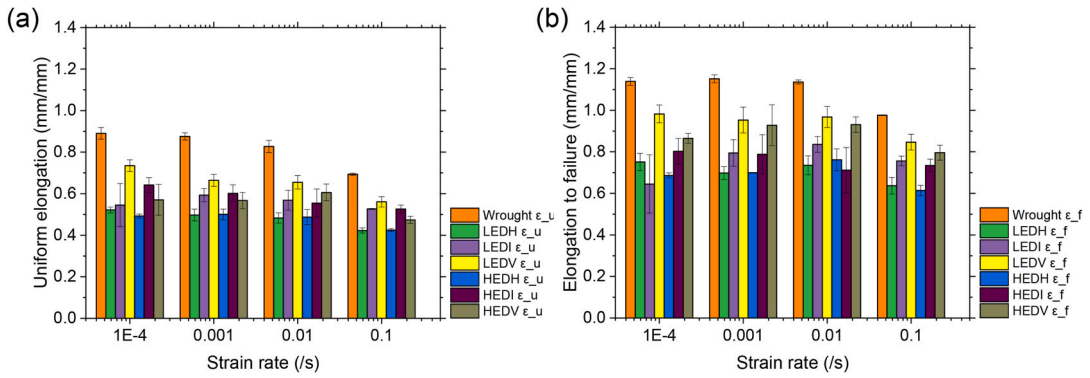

Fig. 7. (a) Uniform elongation and (b) elongation to failure comparison varied at different strain rates for wrought and SLM materials built with LED and HED in three orientations.

Table 5
Uniform elongation (ε_u) and elongation-to-failure (ε_f) in mm/mm at different strain rates for wrought and SLM materials built with LED and HED in three orientations.

Manufacturing state	Strain rate (/s)							
	0.0001		0.001		0.01		0.1	
	ε_u	ε_f	ε_u	ε_f	ε_u	ε_f	ε_u	ε_f
Wrought	0.89 ± 0.03	1.14 ± 0.02	0.88 ± 0.02	1.15 ± 0.02	0.83 ± 0.03	1.14 ± 0.01	0.69 ± 0.00	0.98 ± 0.00
LEDH	0.52 ± 0.01	0.75 ± 0.04	0.50 ± 0.03	0.70 ± 0.03	0.48 ± 0.03	0.74 ± 0.05	0.42 ± 0.01	0.64 ± 0.04
LEDI	0.55 ± 0.10	0.65 ± 0.14	0.59 ± 0.03	0.79 ± 0.06	0.57 ± 0.05	0.84 ± 0.04	0.53 ± 0.00	0.76 ± 0.02
LEDV	0.74 ± 0.03	0.98 ± 0.04	0.66 ± 0.03	0.95 ± 0.06	0.66 ± 0.03	0.97 ± 0.05	0.56 ± 0.02	0.85 ± 0.04
HEDH	0.49 ± 0.01	0.69 ± 0.01	0.50 ± 0.03	0.70 ± 0.00	0.49 ± 0.04	0.76 ± 0.05	0.42 ± 0.01	0.61 ± 0.02
HEDI	0.64 ± 0.04	0.80 ± 0.06	0.60 ± 0.04	0.79 ± 0.09	0.55 ± 0.07	0.71 ± 0.11	0.53 ± 0.02	0.73 ± 0.03
HEDV	0.57 ± 0.07	0.87 ± 0.02	0.57 ± 0.04	0.93 ± 0.10	0.61 ± 0.04	0.93 ± 0.04	0.47 ± 0.02	0.80 ± 0.04

demonstrating consistency with the positive m. The strain rate on SLM SS304L shows a weak dependence as the lower m values fitted with a range from 0.0108 (HEDV) to 0.0162 (LEDI). The dependence of m on build orientation can be revealed by comparing the m determined on different build orientations with two energy densities. It shows the inclined and horizontal orientations have higher m value compared to the vertical orientation. That is, specimens built in 0° and 45° orientation are more sensitive to strain rates. In terms of the effect of energy densities, LED shows a higher m value than HED in inclined and vertical orientations. No visible difference in the horizontal direction can be detected. According to Khodabakhshi et al. [29], the testing temperature and intrinsic structure (i.e., composition, grain structure, and phase morphology) of the material are the two dominant factors controlling the strain rate sensitivity m [29]. They reported an increase in m of SS 410 L compared to SS 316 L stainless steel due to the phase change from martensitic to the austenitic phase where Laser-AM 316 L had a m value of up to ~0.0102 on account of the grain refinement.

4.3. Mechanical property anisotropy

Mechanical anisotropy is defined as $(\sigma_{xy} - \sigma_{yz})/\sigma_{xy}$, where σ_{xy} and σ_{yz} are the yield strength in the horizontal and vertical directions [28]. The mechanical anisotropy calculated in this study is 0.08, 0.07, 0.08, and 0.08 for yield strength of the specimen built with LED assessed from 0.0001/s to 0.1/s, respectively. The value for the HED specimen is 0.11, 0.12, 0.12, and 0.13 for 0.0001/s to 0.1/s, respectively (Table 4). The extent of mechanical anisotropy is dependent on the energy input where the specimens manufactured with a high energy density (e.g., HED) could yield a firmly anisotropic performance. On the contrary, the trend of anisotropy is the opposite for strength and ductility. In terms of the two process parameters employed in this study, specimens printed with LED parameters behave with a slightly higher strength in comparison to specimens printed with HED parameters given that the density of both specimens is higher than 99.0% (Table 3). The difference in grain size and corresponding grain boundary could be one of the reasons for the mechanical anisotropy in varying build orientations. Grain boundaries can behave as a barrier to obstruct crack propagation by deflecting, branching, and blunting the microcracks [29,36,38]. Therefore, with larger grain sizes, effectively less grain boundaries in vertical build orientation, the barriers for crack prorogation are less compared to samples built in horizontal and inclined orientations with the smaller grain sizes. The structures with smaller grain sizes, therefore more effective grain boundaries, are expected to have finer dimple features on the fracture surface, which coincides with the fractography results.

To investigate the effect of grain size, the Hall-Petch relationship was studied. The Hall-Petch relationship describes the correlation between tensile stress with the grain size for polycrystalline alloy [30]. The equation is stated as Eq. (4):

$$YS = \sigma_0 + kD^{-0.5} \tag{4}$$

where σ_0 is the yield stress in the single crystal (friction stress), k is the Hall-Petch coefficient, and D is the grain size. According to the determined average grain size (Table 3) at different manufacturing states and the corresponding yield strength listed in Table 4, a linear regression of the yield strength and inverse square root of the grain dimension is depicted for each strain rate in Fig. 11. During the fitting, outliers on the linear regression could possibly result from the variation in the grain size at a particular build position for the additively manufactured samples [31]. The general trend complies with the Hall-Petch relationship. Higher amount of grain boundaries implies a smaller effective grain size, which reinforces the polycrystalline materials [31–33]. Specimens printed in vertical direction show the largest grain size, hence, behave the weakest strength. LED samples with slightly smaller grain sizes behave moderately higher strengths than those of HED specimens. Grain size variation partially helps to explain the anisotropic performance along different build orientations. Also, during the printing process, the cooling rate decreases away from the baseplate as the build becomes heated, thus leading to a higher dislocation density for the horizontal

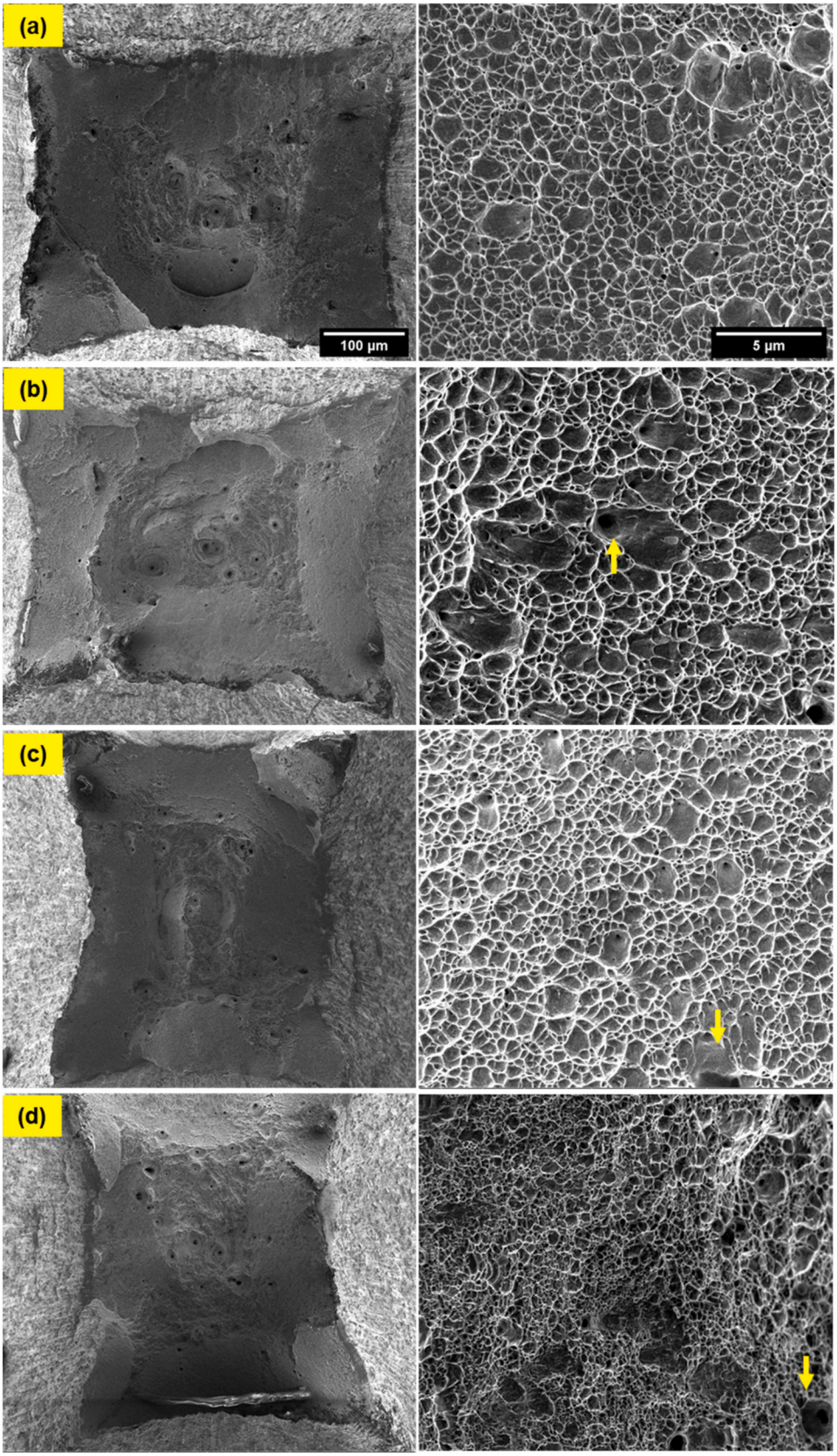

Fig. 8. The same low and high magnification images of tensile fracture surface of wrought material tested at (a) 0.0001/s, (b) 0.001/s, (c) 0.01/s, and (d) 0.1/s.

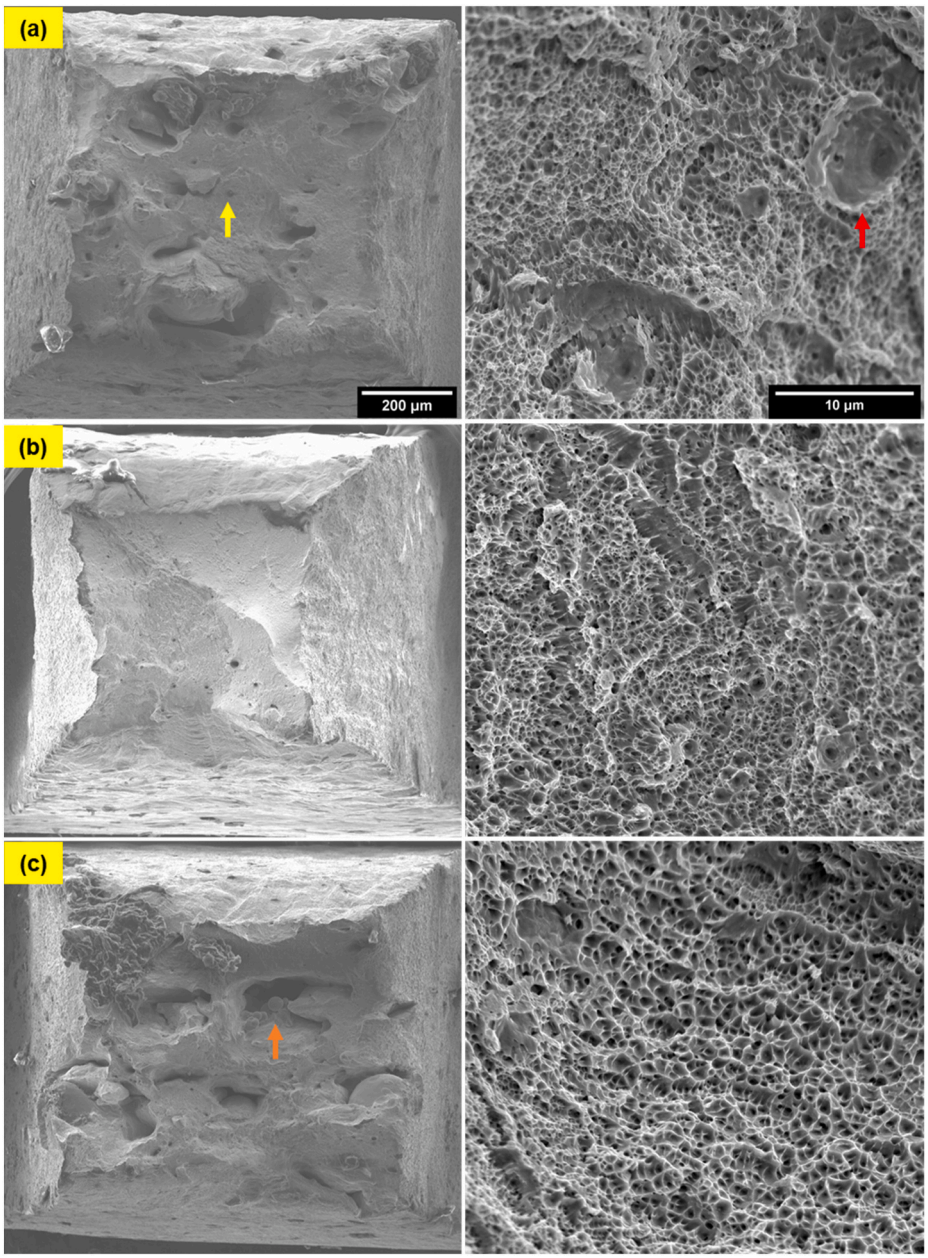

Fig. 9. The same low and high magnification images of the tensile fracture surface of SLM fabricated SS 304 L built with LED in (a) horizontal, (b) inclined, and (c) vertical orientation tested at 0.001/s.

samples built closer to the baseplate, resulting in a higher yield strength [28].

The fitted constitutive parameters σ_0 and k are summarized in Table 7 with acceptable accuracy ($R^2 \geq 0.90$), where k is the grain boundary strengthening parameter. The k value increases from 1466 $MPa{\cdot}\mu m^{0.5}$at 0.0001/s to 1796 $MPa{\cdot}\mu m^{0.5}$at 0.1/s. A similar increasing trend of the Hall-Petch coefficient with strain rate was demonstrated in Ref. [34]. However, Astafurov et al. [27] only observed a slow increase of k value with strain rate (0.0001/s to 0.01/s) up to 2–3%. Astafurov et al. [27] summarized that k ranged from 280 to 410 $MPa{\cdot}\ \mu m^{0.5}$ for Cr–Ni steels with equiaxed grain structures with sizes ranging from few micrometers to hundreds of micrometers. They explained the k value was 695 $MPa{\cdot}\mu m^{0.5}$ in the study of Wang et al. [31] for SS 304, as the substantial non-equiaxed grain structure. A similar non-equiaxed grain morphology can be observed in Figs. 3 and 4, especially for grains in inclined and vertical orientations where the elongated columnar grain morphology is prevalent with a high aspect ratio. The dependence of the k value on the strain rates could also be ascribed to the variation in building parameters and the resulting microstructures, like the distribution and fraction of the defects, grain, and subgrain boundaries. Besides, the Hall-Petch coefficient is dependent on stacking fault energy (SFE). Astafurov et al. [27] demonstrated the k value is higher for the steel with lower SFE. The SFE for the specific material can be determined based on the steel composition in weight percentage, as shown in Eq. (5).

$$SFE\left(mJ\,/\,m^2\right) = -53 + 6.2Ni + 0.7Cr + 3.2Mn + 9.3Mo \tag{5}$$

The SFE determined for SS 304 L in the current study is 25.12 mJ/m^2 according to the chemistry listed in Table 1. σ_0 is identified as a strain-rate sensitive parameter. From Fig. 9, σ_0 (extrapolated stress when $D^{-0.5}$ is zero ideally) seems to rise with the faster strain rate. The estimated σ_0 tabulated in Table 7 demonstrates a generally diminishing trend with a decrease of 14% in strain rate from 0.0001/s to 0.1/s. This value relates

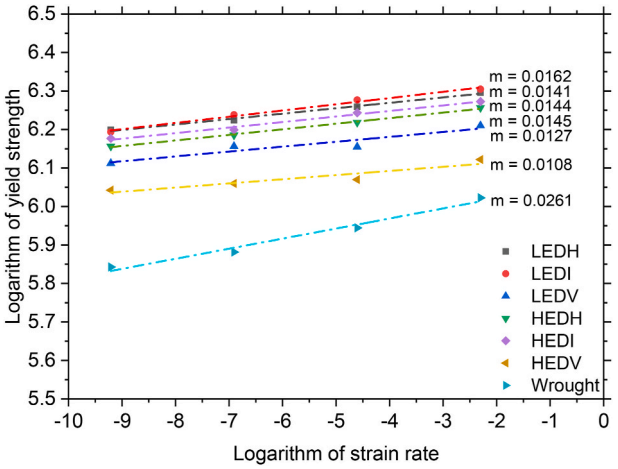

Fig. 10. Strain rate sensitivity (m) of wrought, and SLM material built with LED and HED in horizontal, Inclined, and vertical orientations.

Table 6
The mechanical performance parameters of the examined materials including strain rate sensitivity (m) and work hardness exponent (n) at different strain rates.

Manufacturing state	m	n			
		0.1/s	0.01/s	0.001/s	0.0001/s
Wrought	0.0261 ± 0.0027	0.4809 ± 0.0014	0.4852 ± 0.0007	0.4986 ± 0.0004	0.5023 ± 0.0001
LEDH	0.0141 ± 0.0008	0.3057 ± 0.0005	0.3151 ± 0.0005	0.3129 ± 0.0004	0.3068 ± 0.0004
LEDI	0.0162 ± 0.0012	0.3098 ± 0.0006	0.3230 ± 0.0006	0.3223 ± 0.0005	0.3249 ± 0.0005
LEDV	0.0127 ± 0.0032	0.2743 ± 0.0006	0.2848 ± 0.0006	0.2771 ± 0.0005	0.2808 ± 0.0006
HEDH	0.0145 ± 0.0006	0.3233 ± 0.0006	0.3261 ± 0.0006	0.3308 ± 0.0005	0.3276 ± 0.0005
HEDI	0.0144 ± 0.0012	0.3171 ± 0.0007	0.3379 ± 0.0007	0.3272 ± 0.0006	0.3495 ± 0.0006
HEDV	0.0108 ± 0.0028	0.2969 ± 0.0006	0.3010 ± 0.0006	0.2959 ± 0.0005	0.2969 ± 0.0005

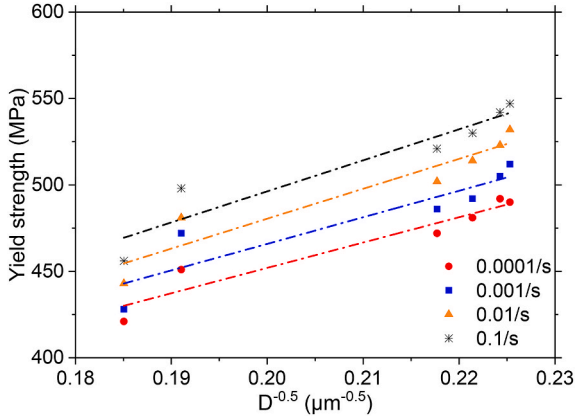

Fig. 11. The relationship between yield strength and grain size for SLM SS 304 L.

to the friction stress, which is required for dislocations to propagate in the crystal lattice for the start of plastic flow [27].

M_{d30} represents the pseudo upper limit for martensite formation. Hence, M_{d30} is determined for the current conventional and SLM SS 304 L to validate if the martensite formation is initiated at the current test temperature. M_{d30} is calculated based on Eq. (1) and the chemical composition listed in Table 1. The value of M_{d30} is between 46.5 °C and −18.9 °C for wrought SS 304 L depending on the variation of the composition of Cr and Ni, which validates the possibility of wrought SS 304 L to promote martensite transformation during plastic deformation. For SLM SS 304 L, the M_{d30} is determined to be 14.9 °C due to the high content of nitrogen (0.06%) in the powder, which acts as an austenite stabilizer. The low M_{d30} temperature for SLM 304 L demonstrates the stable austenitic phase with an absence of martensite transformation at room temperature (test temperature). Wang et al. [11] validated this claim with magnetic permeability measurements and optical microscopy for DED fabricated 304 L with a similar nitrogen content (0.08%) in the powder. To further investigate the nonoccurrence of DIMF in current SS 304 L, Fig. 12 presents the work hardening rate versus the true strain curves tested at a strain rate of 0.0001/s. The slowest strain rate is chosen since it largely reduces the effect of adiabatic heating in comparison to the high strain rates, which could suppress the martensite formation [15]. The occurrence of the second strain hardening behavior implies the existence of deformation-induced martensite, which serves as a substantial barrier for dislocation motion [28]. For the wrought SS 304 L, a slight increase in the work hardening rate is observed where the true strain is over 0.1 mm/mm, which could suggest the DIMF given that the test temperature (room temperature) lies in the range of M_{d30} for wrought material. On the contrary, no secondary work hardening could be identified for SLM SS 304 L in any build conditions. This fact, along with the M_{d30} of 14.9 °C determined for SS 304 L, supports the absence of martensite formation in the material, which leads to a lower work hardening, UTS, and elongation when compared to wrought counterpart, which agrees with the results in the current study. The work hardening rate seems to be smaller in the vertical orientation compared to the horizontal and vertical orientations regardless of energy input, from the zoomed-in image in Fig. 12.

Table 7
Constitutive parameters for Hall-Petch equation at varying strain rates.

$\dot{\varepsilon}$ (/s)	σ_0 (MPa)	k ($MPa{\cdot}\mu m^{0.5}$)	R^2
0.0001	159	1466	0.92
0.001	159	1537	0.91
0.01	134	1731	0.93
0.1	137	1796	0.90

4.4. Strain hardening

The strain hardening exponent (n), also known as the work hard-

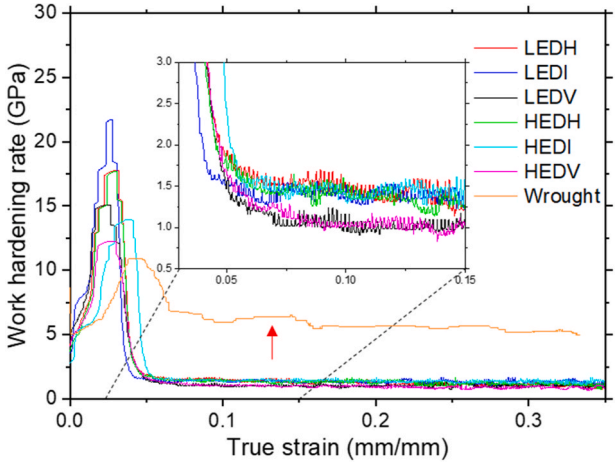

Fig. 12. Work hardening rate versus true strain curves of SLM fabricated SS 304 L in different building conditions at a strain rate of 0.0001/s.

ening exponent, is defined as follows:

$$n = \left(\frac{\partial\, ln\sigma}{\partial\, ln\varepsilon}\right) \tag{6}$$

where the ε is the true plastic strain with the corresponding true stress σ. Using the definition, n can be determined by fitting the linear equation to the logarithmic plots of true stress versus true plastic strain. The physical meaning of the slope is strain hardening exponent n. The determined n of SS 304 L at different manufacturing states with different test speeds are listed in Table 6. Dissimilar to the result presented in Ref. [29] where they observed a higher n for the additive manufacturing state, the wrought SS 304 L performs a higher work hardening exponent, which is consistent with Fig. 5, where the stress-strain curve is steeper in the wrought state than compared to the other relatively flat curve of SLM materials. The work hardening exponent seems to slightly drop with the increasing strain rates from 0.5023 at 0.0001/s to 0.4809 at 0.1/s. No such dependence of strain rates with n can be perceived for SLM SS 304 L. In comparison to the two different energy densities, HED shows slightly higher n. In terms of different building orientations, a higher strain hardening exponent is captured in the horizontal and inclined orientation, similar to the work hardening rate (Fig. 12). The current finding in a true strain range between ~0.10 and 0.25 mm/mm is coincident with Samual's work [35], where the higher work hardening exponent could signify a larger strain hardening rate. In consideration of the microstructure, the larger grain dimensions (in vertical orientation) provide a lower work hardening exponent and strain hardening rate.

4.5. Fractography

The distinct shrinkage in the area of the fracture surface indicates the presence of necking, where the highly localized deformation occurs. From the images with high magnifications, the ductile dimple features can be observed at all strain rates, where the average dimple size seems to be consistent at lower strain rates but becomes smaller at the highest strain rate. A similar conclusion was demonstrated in Ref. [23]. The size of the dimples is related to the area under the tensile stress-strain curve, which is also defined as toughness. The sizes of the dimples are expected to be larger on the fracture surface with a greater area under the curve or toughness [29]. From Fig. 5a, the area under the stress-strain curve is lowest at the highest strain rate (0.1/s), while no noticeable difference is identified at the other three strain rates, which agrees with the statement in Ref. [29].

5. Conclusions

In the current study, the microstructure and mechanical behaviors under different strain rates of SLM fabricated AISI stainless steel 304 L are evaluated in terms of different process parameters (LED and HED) and built orientations (horizontal, inclined, and vertical). The commercial cold-rolled and annealed counterpart was used as a comparison to conventional techniques. Grain structures, tensile strength, elongation-to-failure, anisotropy, strain rate sensitivity, work hardening, and fractographic analysis were carried out on the specimen. The main findings are listed as follows:

1. The densifications of the specimen printed with both LED and HED are more than 99% dense. The average grain sizes were determined along the horizontal, inclined, and vertical orientation for both LED and HED. A relatively stronger texture along the build direction is observed for HED due to the non-uniform grain distributions with the high energy input.
2. Yield strength improves with increasing strain rates. Higher yield strength is observed for SLM SS 304 L than that of wrought material. The increasing trend of UTS with strain rates fades at a higher strain rate as the occurrence of inhomogeneous plastic deformation (as suggested by Zhuo et al. [26]) gives rise to the insensitivity of UTS on strain rate at higher test speeds. Elongation-to-failure reduces with the increasing strain.
3. Wrought SS 304 L has the highest strain rate sensitivity (m = ~0.0261) compared to SLM SS 304 L. For SLM material, the horizontal and inclined orientations possess higher m values compared to the vertical orientation, which demonstrates they are more sensitive to the strain rates. The difference in grain dimension could initiate this variation in strain rate sensitivity as the larger grain size is determined for the vertical orientations regardless of energy input.
4. The mechanical anisotropy depends on the energy input where a high energy density (e.g., HED) could yield a strict anisotropic performance. The Hall-Petch relationship is validated for this study, which states that the samples with larger grain sizes have a lower tensile strength. The Hall-Petch coefficient increases from 1466 $MPa{\cdot}\mu m^{0.5}$at 0.0001/s to 1796 $MPa{\cdot}\mu m^{0.5}$at 0.1/s possibly due to non-equiaxed grain morphology. σ_0 seems to rise with the fast strain rate. On the contrary, the trend of anisotropy is the opposite for strength and ductility.
5. Powder with a high content of nitrogen stabilizes the austenite. Hence no secondary work hardening of DIMD is observed from the work hardening rate curve. The strain hardening exponent and work hardening rate are positively correlated, which is negatively associated with the grain dimension.
6. The dimple features indicate the ductile fracture mode at all strain rates, where the average dimple size seems to become smaller at the highest strain rate. For SLM material, the smaller dimple size is observed in horizontal and inclined orientations due to the more effective grain boundaries behaving as barriers to obstruct the crack propagation.

Data availability

The raw/processed data required to reproduce these findings cannot be shared at this time as the data also forms part of an ongoing study.

CRediT authorship contribution statement

Tan Pan: Conceptualization, Methodology, Investigation, Writing – original draft. **Xinchang Zhang:** Writing – review & editing, Visualization. **Aaron Flood:** Writing – review & editing, Formal analysis. **Sreekar Karnati:** Methodology. **Wei Li:** Writing – review & editing-Writing- Reviewing and Editing. **Joseph Newkirk:** Supervision, Writing – review & editingReviewing and Editing. **Frank Liou:** Supervision, Funding acquisition.

Declaration of competing interest

The authors declare that they have no known competing financial interests or personal relationships that could have appeared to influence the work reported in this paper.

Acknowledgment

This project was supported by Honeywell Federal Manufacturing & Technologies under Contract No. DE-NA0002839 with the U.S. Department of Energy, National Science Foundation Grants CMMI 1625736, Department of Energy Grant #DE-SC0018879, Intelligent Systems Center, Manufacturing Engineering program, and Material Research Center at Missouri S&T. Their financial support is greatly appreciated.

References

[1] K. Abd-Elghany, D.L. Bourell, Property evaluation of 304L stainless steel fabricated by selective laser melting, Rapid Prototyp. J. 18 (2012) 420–428, https://doi.org/10.1108/13552541211250418.

[2] X. Zhang, T. Pan, W. Li, F. Liou, Experimental characterization of a direct metal deposited cobalt-based alloy on tool steel for component repair, JOM 71 (2019), https://doi.org/10.1007/s11837-018-3221-5.

[3] A. Saboori, A. Aversa, G. Marchese, S. Biamino, M. Lombardi, P. Fino, Application of directed energy deposition-based additive manufacturing in repair, Appl. Sci. 9 (2019), https://doi.org/10.3390/app9163316.

[4] B.E. Carroll, R.A. Otis, J.P. Borgonia, J.O. Suh, R.P. Dillon, A.A. Shapiro, D. C. Hofmann, Z.K. Liu, A.M. Beese, Functionally graded material of 304L stainless steel and inconel 625 fabricated by directed energy deposition: characterization and thermodynamic modeling, Acta Mater. 108 (2016) 46–54, https://doi.org/10.1016/j.actamat.2016.02.019.

[5] T. Pan, X. Zhang, T. Yamazaki, A. Sutton, W. Cui, L. Li, F. Liou, Characteristics of Inconel 625 — copper bimetallic structure fabricated by directed energy deposition, Int. J. Adv. Manuf. Technol. 625 (2020) 1261–1274, https://doi.org/10.1007/s00170-020-05713-z.

[6] E. Liverani, S. Toschi, L. Ceschini, A. Fortunato, Effect of selective laser melting (SLM) process parameters on microstructure and mechanical properties of 316L austenitic stainless steel, J. Mater. Process. Technol. 249 (2017) 255–263, https://doi.org/10.1016/j.jmatprotec.2017.05.042.

[7] T. Pan, S. Karnati, Y. Zhang, X. Zhang, C.-H. Hung, L. Li, F. Liou, Experiment characterization and formulation estimation of tensile properties for selective laser melting manufactured 304L stainless steel, Mater. Sci. Eng. (2020) 140086, https://doi.org/10.1016/j.msea.2020.140086.

[8] P. Deng, Q. Peng, E.H. Han, W. Ke, C. Sun, Z. Jiao, Effect of irradiation on corrosion of 304 nuclear grade stainless steel in simulated PWR primary water, Corrosion Sci. 127 (2017) 91–100, https://doi.org/10.1016/j.corsci.2017.08.010.

[9] K. Guan, Z. Wang, M. Gao, X. Li, X. Zeng, Effects of processing parameters on tensile properties of selective laser melted 304 stainless steel, Mater. Des. 50 (2013) 581–586, https://doi.org/10.1016/j.matdes.2013.03.056.

[10] Q.B. Nguyen, Z. Zhu, F.L. Ng, B.W. Chua, S.M.L. Nai, J. Wei, High mechanical strengths and ductility of stainless steel 304L fabricated using selective laser melting, J. Mater. Sci. Technol. 35 (2019) 388–394, https://doi.org/10.1016/j.jmst.2018.10.013.

[11] Z. Wang, T.A. Palmer, A.M. Beese, Effect of Processing Parameters on Microstructure and Tensile Properties of Austenitic Stainless Steel 304L Made by Directed Energy Deposition Additive Manufacturing, vol. 110, Elsevier Ltd, 2016.

[12] M.W. Bowkett, S.R. Keown, D.R. Harries, Quench- and deformation-induced structures in two austenitic stainless steels, Met. Sci. 16 (1982) 499–517, https://doi.org/10.1179/030634582790427082.

[13] J. Talonen, PhD, Effect of Strain-Induced Alfa'-Martensite Transformation on Mechanical Properties of Metastable Austenitic Stainless Steels, 2007, ISBN 9789512287796.

[14] J. Talonen, P. Nenonen, G. Pape, H. Hänninen, Effect of strain rate on the strain-induced γ, → α′-martensite transformation and mechanical properties of austenitic stainless steels, Metall. Mater. Trans. A Phys. Metall. Mater. Sci. 36 (2005) 421–432, https://doi.org/10.1007/s11661-005-0313-y. *A*.

[15] J.A. Lichtenfeld, C.J. Van Tyne, M.C. Mataya, Effect of strain rate on stress-strain behavior of alloy 309 and 304L austenitic stainless steel, Metall. Mater. Trans. 37 (2006) 147–161, https://doi.org/10.1007/s11661-006-0160-5.

[16] T. Angel, Formation of martensite in austenitic stainless steels, effect of deformation, temperature and composition, J. Iron Steel Inst. (1954) 165–174.

[17] G.B. Olson, M. Azrin, Transformation behavior of TRIP steels, Metall. Trans. A 9 (1978) 713–721, https://doi.org/10.1007/BF02659928.

[18] A. Rosen, R. Jago, T. Kjer, Tensile properties of metastable stainless steels, J. Mater. Sci. 7 (1972) 870–876, https://doi.org/10.1007/BF00550434.

[19] J.P. Bressanelli, A. Moskowitz, Effects of strain rate, temperature, and composition on tensile properties of metastable austenitic stainless steels, ASM Trans Quart 59 (1966) 223–239.

[20] L.E. Murr, K.P. Staudhammer, S.S. Hecker, M.G. Stout, K.P. Staudhammer, L. E. Murr, J.L. Smith, Effects of strain state and strain rate on deformation-induced transformation in 304 stainless steel : Part 1 . Microstructural study, Metall. Trans. A 13 (1982) 627–635, https://doi.org/10.1007/BF02644428.

[21] M.M. Parvez, T. Pan, Y. Chen, S. Karnati, J.W. Newkirk, F. Liou, High cycle fatigue performance of lpbf 304l stainless steel at nominal and optimized parameters, Materials 13 (2020) 1–15, https://doi.org/10.3390/ma13071591.

[22] T. Kurzynowski, K. Gruber, W. Stopyra, B. Kuźnicka, E. Chlebus, Correlation between process parameters, microstructure and properties of 316 L stainless steel processed by selective laser melting, Mater. Sci. Eng. 718 (2018) 64–73, https://doi.org/10.1016/j.msea.2018.01.103.

[23] Z. Li, T. Voisin, J.T. McKeown, J. Ye, T. Braun, C. Kamath, W.E. King, Y.M. Wang, Tensile properties, strain rate sensitivity, and activation volume of additively manufactured 316L stainless steels, Int. J. Plast. 120 (2019) 395–410, https://doi.org/10.1016/j.ijplas.2019.05.009.

[24] S. Karnati, I. Axelsen, F.F. Liou, J.W.N. Investigation of, Tensile properties of bulk and slm fabricated 304L stainless steel using various gage length specimens, Solid Free. Fabr. 13 (2016).

[25] T. DebRoy, H.L. Wei, J.S. Zuback, T. Mukherjee, J.W. Elmer, J.O. Milewski, A. M. Beese, A. Wilson-Heid, A. De, W. Zhang, Additive manufacturing of metallic components – process, structure and properties, Prog. Mater. Sci. 92 (2018) 112–224, https://doi.org/10.1016/j.pmatsci.2017.10.001.

[26] Z. Zhuo, S. Xia, Q. Bai, B. Zhou, The effect of grain boundary character distribution on the mechanical properties at different strain rates of a 316L stainless steel, J. Mater. Sci. 53 (2018) 2844–2858, https://doi.org/10.1007/s10853-017-1695-0.

[27] S.V. Astafurov, G.G. Maier, E.V. Melnikov, V.A. Moskvina, M.Y. Panchenko, E. G. Astafurova, The strain-rate dependence of the Hall-Petch effect in two austenitic stainless steels with different stacking fault energies, Mater. Sci. Eng. 756 (2019) 365–372, https://doi.org/10.1016/j.msea.2019.04.076.

[28] Z. Zhu, W. Li, Q.B. Nguyen, X. An, W. Lu, Z. Li, F.L. Ng, S.M. Ling Nai, J. Wei, Enhanced strength–ductility synergy and transformation-induced plasticity of the selective laser melting fabricated 304L stainless steel, Addit. Manuf. 35 (2020) 101300, https://doi.org/10.1016/j.addma.2020.101300.

[29] F. Khodabakhshi, M.H. Farshidianfar, A.P. Gerlich, M. Nosko, V. Trembošová, A. Khajepour, Microstructure, strain-rate sensitivity, work hardening, and fracture behavior of laser additive manufactured austenitic and martensitic stainless steel structures, Mater. Sci. Eng. 756 (2019) 545–561, https://doi.org/10.1016/j.msea.2019.04.065.

[30] K.K. Singh, S. Sangal, G.S. Murty, Hall-Petch behaviour of 316L austenitic stainless steel at room temperature, Mater. Sci. Technol. 18 (2002) 165–172, https://doi.org/10.1179/026708301125000384.

[31] Z. Wang, T.A. Palmer, A.M. Beese, Effect of processing parameters on microstructure and tensile properties of austenitic stainless steel 304L made by directed energy deposition additive manufacturing, Acta Mater. 110 (2016) 226–235, https://doi.org/10.1016/j.actamat.2016.03.019.

[32] K.K. Singh, Strain hardening behaviour of 316L austenitic stainless steel, Mater. Sci. Technol. 20 (2004) 1134–1142, https://doi.org/10.1179/026708304225022089.

[33] H. Yu, J. Yang, J. Yin, Z. Wang, X. Zeng, Comparison on mechanical anisotropies of selective laser melted Ti-6Al-4V alloy and 304 stainless steel, Mater. Sci. Eng. 695 (2017) 92–100, https://doi.org/10.1016/j.msea.2017.04.031.

[34] V.E. Panin, R.W. Armstrong, Hall-Petch analysis for temperature and strain rate dependent deformation of polycrystalline lead, Phys. Mesomech. 19 (2016) 35–40, https://doi.org/10.1134/S1029959916010045.

[35] K.G. Samuel, Limitations of Hollomon and Ludwigson stress-strain relations in assessing the strain hardening parameters, J. Phys. D Appl. Phys. 39 (2006) 203–212, https://doi.org/10.1088/0022-3727/39/1/030.

[36] Z. Lee, V. Radmilovic, B. Ahn, E.J. Lavernia, S.R. Nutt, Tensile deformation and fracture mechanism of bulk bimodal ultrafine-grained Al-Mg alloy, Metall. Mater. Trans. A Phys. Metall. Mater. Sci. 41 (2010) 795–801, https://doi.org/10.1007/s11661-009-0007-y.

[37] E.J. Lavernia, T.S. Srivatsan, F.A. Mohamed, Strength, deformation, fracture behaviour and ductility of aluminium-lithium alloys, J. Mater. Sci. 25 (1990) 1137–1158, https://doi.org/10.1007/BF00585420.

[38] X. Wang, B. Zheng, K. Yu, S. Jiang, E.J. Lavernia, J.M. Schoenung, The role of cell boundary orientation on mechanical behavior: a site-specific micro-pillar characterization study, Additive Manufacturing 46 (2021) 102154.

[39] T. Pan, Influence of Input Energy on Mechanical Properties of Laser Powder Bed Fused AISI 304L Stainless Steel, Missouri University of Science and Technology, 2020.